Made available through Montana State University's ScholarWorks

Thermal properties of single-layer MoS2–WS2 alloys enabled by machine-learned interatomic potentials

Juan M. Marmolejo-Tejada, Martín A. Mosquera

Copyright Royal Society of Chemistry 2022

Journal Name

ARTICLE TYPE

Cite this: DOI: 00.0000/xxxxxxxxxx

Thermal properties of single-layer MoS_2-WS_2 alloys enabled by machine-learned interatomic potentials

Juan M. Marmolejo-Tejada,[a] and Martín A. Mosquera*[a]

Received Date
Accepted Date

DOI: 00.0000/xxxxxxxxxx

Two-dimensional (2D) quantum materials are poised to transform conventional electronics for a wide spectrum of applications that will encompass chemical sciences. For the study of thermal transport in single-layer (1L) or multi-layer transition metal dichalcogenides (TMDs), this work explores the combination of density functional theory (DFT) and algorithmic training for the generation of a moment tensor potential (MTP) that models 1L-MoS_2, 1L-WS_2 and their alloys, and demonstrates a synergy of theoretical techniques that is anticipated to play an important role in the field. From a high-performance computing perspective, these yield very convenient inter-atomic (or inter-molecular in other contexts) potentials that serve useful to predict the response of quantum materials to thermal perturbations, or other driving forces. We show that our trained MTP functions successfully describe vibrational properties of the systems, and their thermal conductivities. The trained potential displays consistent agreement with DFT calculations, as well as the Stillinger-Weber (SW) potential. We also find that the thermal conductivity of the 2D alloys is lowly affected by sulfur vacancies. This is a behavior that may aid the fine-tuning of material's thermal properties for heat management and energy storage and conversion applications.

Transition metal dichalcogenides (TMDs) are layered two-dimensional (2D) crystalline structures with outstanding electronic and optical properties that have been identified as promising materials for the development of novel nanoelectronic devices, for which accurate estimations of materials' thermal transport properties are essential for thermal management and energy storage/conversion applications [1–9]. Structural defects, such as vacancies, usually play a significant role in the electron and thermal transport properties of these devices, which could result in significant lattice distortions in the vicinity of the defect and hinder phonon transport properties [9–11]. These systems usually require the preparation of atomistic models with very large number of atoms (in the order of thousands, or more), for which first-principles methods, such as density functional theory (DFT), become prohibitively expensive in terms of computational costs.

Recently, machine-learned interatomic potentials (MLIPs) have been explored for modeling large-scale molecular systems with high accuracy and significantly lower computational cost than first-principles methods [12,13]. Although these potentials usually have very low transferability, they have a flexible functional form and can be systematically improved by increasing the training set and number of basis functions, but at the expense of higher computational cost [12,14–17]. Moment tensor potentials (MTPs) describe atomic local environments throughout rotationally covariant tensors (formally, the moment of inertia) [12] and have shown to provide high accuracy and performance, when compared to competing MLIP models in the literature [17], and are expected to help understand the effects of structural and substitutional defects in the performance of TMD-based nanoelectronic devices [13,18].

Non-equilibrium molecular dynamics (NEMD) methods have been used for estimating the thermal conductivity, κ, of semiconductor materials due to their direct analogy to experimental procedures [10]. For this purpose, the central/scattering region is connected to two semi-infinite, defect-free regions, labeled as heat source and drain terminals, respectively. Then, the momentum of the hottest atom in the drain is exchanged with the momentum of the coldest atom in the source, although conserving the total energy and momentum of the system [20,21]. This produces a heat current from source to drain that results in a temperature gradient along the length of the system.

Alternatively, the non-equilibrium Green's function (NEGF) method has also been employed for calculating thermal conductance, σ, by obtaining the phonon transmission spectrum from the phonon Green's function $G(\omega)$ [22] and calculate $\kappa = \sigma l/S$, where l is the length of the sample and S is the cross-sectional area [23].

This work aims at getting a better understanding of the effects of structural and substitutional defects in the performance of nanoelectronic devices and may also provide a tool for phononic engineering by controllably manipulating the thermal and elec-

[a] Department of Chemistry and Biochemistry, Montana State University, Bozeman, MT 59717 USA; E-mail: martinmosquera@montana.edu

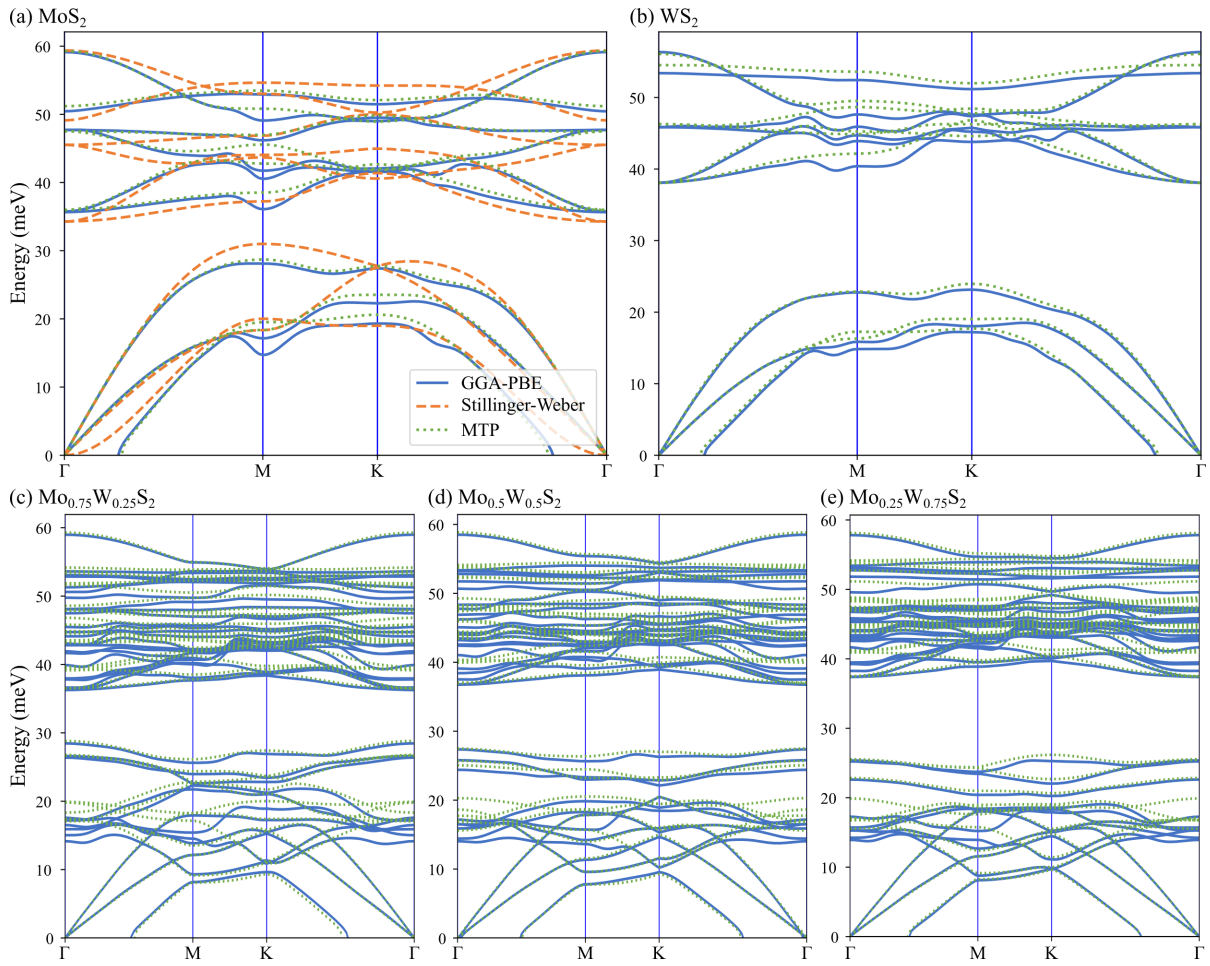

Fig. 1 Validation of the trained MTPs: Comparison of different potentials for the determination of phonon dispersion diagrams for 1L- (a) MoS_2, (b) WS_2, (c) $Mo_{0.75}W_{0.25}S_2$, (d) $Mo_{0.5}W_{0.5}S_2$ and (e) $Mo_{0.25}W_{0.75}S_2$. These diagrams are calculated with our trained MTP (green-dotted lines) and compared to DFT calculations (solid blue lines). Panel (a) also includes the phonon dispersion of 1L-MoS_2 obtained with the SW potential in [19] (orange-dashed lines).

trical conductivity properties of nanostructured devices [24], where defect engineering may become a necessary step in finely tuning the thermoelectric properties of these devices [8,10,25].

Similar to Mortazavi *et al.* [6,11], we passively train our potential, but include the pristine and alloyed configurations in the training set. This consists of 780 1L configurations from small random atomic displacements and molecular dynamics (MD) trajectories, as detailed in our Supporting Information.

To assess the accuracy of our trained MTP, we compute vibrational modes and phonon band diagrams with the supercell method [26–28]. For this, we diagonalize the dynamical matrix, which is constructed by small point displacements to the relaxed geometries. We use $21\times21\times1$ repetitions for 1L-MoS_2 and WS_2, and $11\times11\times1$ repetitions for the 1L-$Mo_xW_{1-x}S_2$ alloys. Then, we calculate the finite differences of the forces with the central finite difference method, using 0.01 Å atomic displacements and 1×10^{-8} Hartree/Bohr^2 force tolerance, as implemented in QuantumATK [29,30].

Figure 1 shows the computed phonon band structure diagrams for the 1L-$Mo_xW_{1-x}S_2$ systems. We find very good agreement between DFT calculations and our MTP. This includes capturing a "negative" energy band at the Γ point in both DFT and MTP calculations; the negative band results from benign computational artifacts and do not translate into any anomalous instability [9,11,31,32]. We verify this by fully relaxing the 1L-MoS_2 and WS_2 unit cells (see Figure S2), where the imaginary frequencies disappear, also noting that the frequency of the optical modes is reduced by $\sim 20-30cm^{-1}$ with the functional and self-consistent criteria that were used in this study. Interestingly, our trained MTP agrees well with the lattice parameters of the relaxed structures and the resulting phonon band diagrams. To further improve the accuracy of calculations one can add MD trajectories at higher temperatures, relax the unit cells for stress, and increase the accuracy of the reference DFT calculations. However, the random displacement method is sufficient for the modeling performed in this work.

For additional reference, we also compute the phonon dispersion diagram of 1L-MoS_2 with the Stillinger-Weber (SW) potential in [19] (see Figure 1(a)) and compare the optical vibrational modes in Figure 2(a), finding good agreement with our trained MTP. Furthermore, we verify the evolution of the optical vibrational modes of the compositional-dependent $Mo_xW_{1-x}S_2$ systems in

Figure 2(b). Consistent with our previous work in [33], we observe a blue-shift of the A"$_2$ mode (at 477 and 454 cm^{-}1 for pristine 1L-MoS_2 and WS_2, respectively) and red-shift of the E" mode (at 288 and 307 cm^{-}1 for pristine 1L-MoS_2 and WS_2, respectively) with increased Mo content.

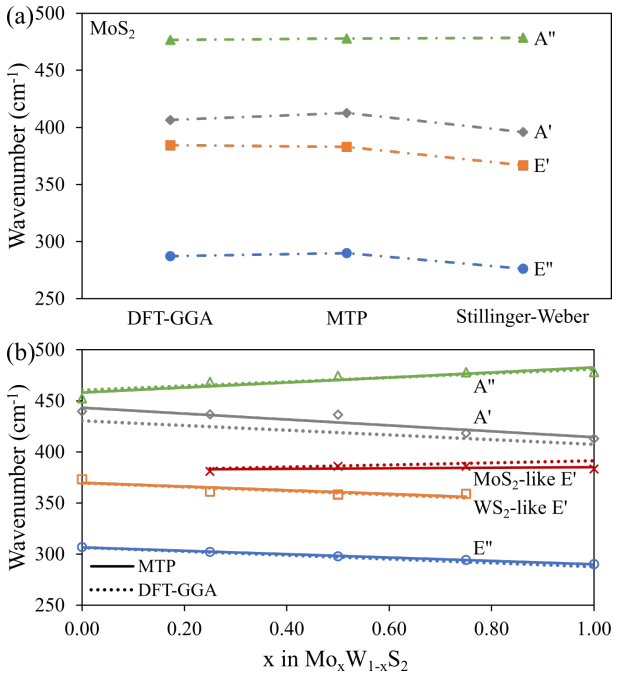

Fig. 2 (a) Optical vibrational modes of 1L-MoS_2 obtained with our trained MTP and SW potential in [19], and compared to DFT calculations. (b) Evolution of the optical absorption spectra for the 1L-$Mo_xW_{1-x}S_2$ structures, estimated with our trained MTP (symbols and solid lines) and compared to DFT calculations (dotted lines).

Our inter-atomic potential was then used for estimating the thermal conductivity of 1L-MoS_2, WS_2 and their alloys, for which we consider sharp and alloy interfaces, as depicted in Figure 3(a). We setup system configurations of length l = 16, 33, 66 and 132 nm for all cases. For S, we used a fixed width of 25.3 nm for NEMD and 7.58 nm for NEGF calculations (due to larger computational complexity) and assumed a monolayer thickness of 0.6033 nm [34].

The conventional approach for estimating the thermal conductivity of infinite systems, κ_∞ consists in extrapolating the thermal conductivity results of finite lengths, $1/\kappa = (1+\Lambda/l)/\kappa_\infty$ [1,6,35], where l is the length of the sample and Λ is the effective phonon mean free path, assumed to be 100 nm in all cases.

As summarized in Table S3, previous measurements of κ for 1L-MoS_2 at 300K range between 34.5±4 and 84±17 WK^{-1}m^{-1} [36–38], while theoretical values range between 1.35 and 131 WK^{-1}m^{-1}, where several methods have been employed, including the self-consistent solution of the Boltzman transport equation (BTE) [28,34,39], the solution of Slack expression for the acoustic phonon modes [40], in addition to the NEMD [41–43] and NEGF [23] methods. Our MTP calculations result in κ of 43.2 and 63.4 WK^{-1}m^{-1} with the NEMD and NEGF methods, respectively, showing very good agreement with the range of experimental values and our analogous calculations with the SW potential. Our results of finite-length calculations and extrapolation of infinite-length κ are shown in Figure 3(b).

Figure 3(c) compares κ for the 1L-$Mo_xW_{1-x}S_2$ systems using the NEMD method. For 1L-WS_2, there is only one reference experimental result for κ to the best of our knowledge, 32 WK^{-1}m^{-1} [44], that is lower than the experimental references for MoS_2. Our MTP calculations result in κ of 33.7 and 51.4 WK^{-1}m^{-1} with the NEMD and NEGF methods, respectively, noting that the NEMD result is in better agreement with the experimental value and reference calculations with the Slack expression [40]. Then, we verify that 1L-MoS_2 has higher κ than 1L-WS_2, which is also related to its lower average atomic mass [40].

Furthermore, we observe that κ for sharp interfaces is lower than that of the pristine materials, where $Mo_{0.5}W_{0.5}S_2$ has the lower value among the studied concentrations. Alloy interfaces have slightly lower κ and have very low variability among the cases considered in this study, as shown in the inset of Figure 3(c). This could be useful for engineering the thermal transport properties of other alloy configurations, independent of content concentrations.

Lastly, we add S vacancies to our systems and compute κ for small defect concentrations and a fixed l =66 nm. As observed in Figure 3(d), κ is reduced between 25-45% for the pristine materials with a defect density of 0.5%. This is consistent with previous studies where it was observed that vacancies in few-layer MoS_2 produced a sharp decrease in κ, that drops even further with increasing defect concentrations due to phonon-defect scattering [25], but noting that very large defect densities result in a transition from crystalline to an amorphous structures [25]. In the other hand, alloy structures are more resilient to S vacancies, with as much as 13% reduction in κ at 0.5% defect density.

We have shown that MTPs can accurately reproduce phononic structure and thermal transport properties of pristine and alloyed 1L-TMDs. Although we find distinctive phonon spectrum features for 1L-$Mo_xW_{1-x}S_2$ alloys at different concentrations, we observe that thermal transport properties have very low dependence on the alloy content, making it possible to engineer the thermal transport properties of similar materials by mixing different atomic species. Furthermore, we found that alloy configurations are more resilient to S vacancies, providing new opportunities for the fabrication of novel devices without much dependence on costly techniques for obtaining defect-free crystalline materials. Lastly, precision largely depends on the reference DFT method and training set, making it possible to obtain reasonable results without the need of long optimization sequences and higher computational costs [6,11]. Future work includes the application of MTPs to multilayer systems and other related quantum materials.

The authors thank Montana State University, Bozeman, for startup support and computational resources within the Tempest Research Cluster, and the Synopsys' QuantumATK development team for helpful discussions. M.A.M. acknowledges support from the MonArk NSF Quantum Foundry supported by the National Science Foundation Q-AMASE-i program under NSF award No. DMR-1906383.

There are no conflicts to declare.

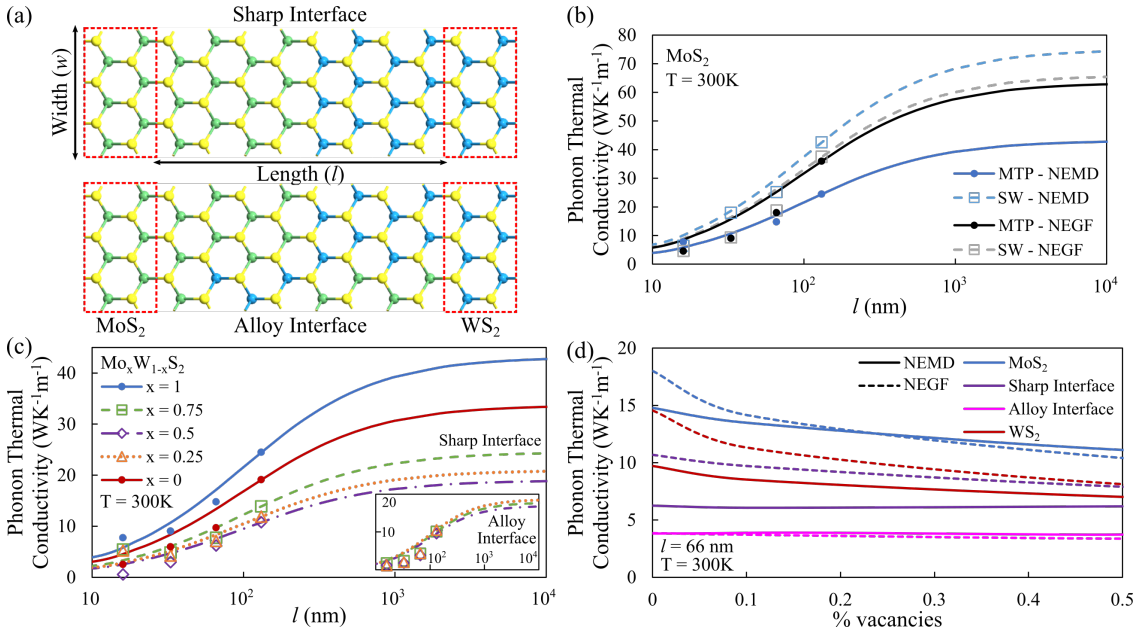

Fig. 3 (a) Top view of the 1L-MoS_2/WS_2 heterostructure with sharp or alloy interface. Blue, green and yellow spheres correspond to W, Mo and S atoms, respectively. (b) Phonon thermal conductivity of 1L-MoS_2 at $T = 300K$ as a function of length, using the NEMD and NEGF methods. Our calculations with the trained MTP (solid lines) are compared to calculations with the SW potential (dashed lines) in [19]. (c) Phonon thermal conductivity of 1L-Mo_xW1-xS_2 systems at $T = 300K$ as a function of length, obtained with our trained MTP and the NEMD method. The infinite thermal conductivity, κ_∞, in panels (b) and (c) is estimated from the finite length results, assuming a phonon mean free path $\Lambda = 100$ nm for all systems. (d) Effect of sulfur vacancies on the thermal conductivity of 1L-MoS_2, WS_2 and $Mo_{0.5}W_{0.5}S_2$ systems. Alloy interfaces show little variations in the estimated κ with both the NEMD (solid lines) and NEGF (dashed lines) methods.

References

1 P. K. Schelling, S. R. Phillpot and P. Keblinski, *Physical Review B*, 2002, **65**, 144306.
2 J. D. Renteria, D. L. Nika and A. A. Balandin, *Applied Sciences*, 2014, **4**, 525–547.
3 S. Sun, M. K. Samani, Y. Fu, T. Xu, L. Ye, M. Satwara, K. Jeppson, T. Nilsson, L. Sun and J. Liu, *Advanced Materials Interfaces*, 2018, **5**, 1800318.
4 A. Nylander, Y. Fu, M. Huang and J. Liu, *IEEE Transactions on Components, Packaging and Manufacturing Technology*, 2019, **9**, 427–433.
5 Y. Fu, J. Hansson, Y. Liu, S. Chen, A. Zehri, M. K. Samani, N. Wang, Y. Ni, Y. Zhang, Z.-B. Zhang, Q. Wang, M. Li, H. Lu, M. Sledzinska, C. M. S. Torres, S. Volz, A. A. Balandin, X. Xu and J. Liu, *2D Materials*, 2019, **7**, 012001.
6 B. Mortazavi, E. V. Podryabinkin, I. S. Novikov, S. Roche, T. Rabczuk, X. Zhuang and A. V. Shapeev, *JPhys Materials*, 2020, **3**, 02LT02.
7 G. Bouzerar, S. Thébaud, S. Pecorario and C. Adessi, *Journal of Physics: Condensed Matter*, 2020, **32**, 295702.
8 A. J. Islam, M. S. Islam, N. Ferdous, J. Park and A. Hashimoto, *Physical Chemistry Chemical Physics*, 2020, **22**, 13592–13602.
9 H. Zhan, Y. Nie, Y. Chen, J. M. Bell and Y. Gu, *Advanced Functional Materials*, 2020, **30**, 1903841.
10 Y. Lee, S. Lee and G. S. Hwang, *Physical Review B*, 2011, **83**, 125202.
11 B. Mortazavi, I. S. Novikov, E. V. Podryabinkin, S. Roche, T. Rabczuk, A. V. Shapeev and X. Zhuang, *Applied Materials Today*, 2020, **20**, 100685.
12 A. V. Shapeev, *Multiscale Modeling and Simulation*, 2016, **14**, 1153–1173.
13 V. V. Ladygin, P. Y. Korotaev, A. V. Yanilkin and A. V. Shapeev, *Computational Materials Science*, 2020, **172**, 109333.
14 J. Behler, *The Journal of Chemical Physics*, 2016, **145**, 170901.
15 I. I. Novoselov, A. V. Yanilkin, A. V. Shapeev and E. V. Podryabinkin, *Computational Materials Science*, 2019, **164**, 46–56.
16 C. Nyshadham, M. Rupp, B. Bekker, A. V. Shapeev, T. Mueller, C. W. Rosenbrock, G. Csányi, D. W. Wingate and G. L. W. Hart, *npj Computational Materials*, 2019, **5**, 51.
17 Y. Zuo, C. Chen, X. Li, Z. Deng, Y. Chen, J. Behler, G. Csányi, A. V. Shapeev, A. P. Thompson, M. A. Wood and S. P. Ong, *Journal of Physical Chemistry A*, 2020, **124**, 731–745.
18 I. S. Novikov, K. Gubaev, E. V. Podryabinkin and A. V. Shapeev, *Machine Learning: Science and Technology*, 2021, **2**, 025002.
19 J.-W. Jiang, H. S. Park and T. Rabczuk, *Journal of Applied Physics*, 2013, **114**, 064307.
20 F. Müller-Plathe, *The Journal of chemical physics*, 1997, **106**, 6082–6085.
21 C. Nieto-Draghi and J. B. Avalos, *Molecular Physics*, 2003, **101**, 2303–2307.
22 T. Markussen, A.-P. Jauho and M. Brandbyge, *Phys. Rev. B*, 2009, **79**, 035415.
23 Y. Cai, J. Lan, G. Zhang and Y.-W. Zhang, *Physical Review B*, 2014, **89**, 035438.
24 G. Xie, Y. Shen, X. Wei, L. Yang, H. Xiao, J. Zhong and G. Zhang, *Scientific reports*, 2014, **4**, 1–6.
25 A. Aiyiti, S. Hu, C. Wang, Q. Xi, Z. Cheng, M. Xia, Y. Ma, J. Wu, J. Guo, Q. Wang *et al.*, *Nanoscale*, 2018, **10**, 2727–2734.
26 D. Alfè, *Computer Physics Communications*, 2009, **180**, 2622–2633.
27 A. Togo, F. Oba and I. Tanaka, *Physical Review B*, 2008, **78**, 134106.
28 A. N. Gandi and U. Schwingenschlögl, *EPL (Europhysics Letters)*, 2016, **113**, 36002.
29 *QuantumATK version S-2021.06-SP1, Synopsys QuantumATK (https://www.synopsys.com/silicon/quantumatk.html)*.
30 S. Smidstrup, T. Markussen, P. Vancraeyveld, J. Wellendorff, J. Schneider, T. Gunst, B. Verstichel, D. Stradi, P. A. Khomyakov, U. G. Vej-Hansen, M. E. Lee, S. T. Chill, F. Rasmussen, G. Penazzi, F. Corsetti, A. Ojanperä, K. Jensen, M. L. Palsgaard, U. Martinez, A. Blom, M. Brandbyge and K. Stokbro, *Journal of Physics Condensed Matter*, 2020, **32**, year.
31 V. N. Popov and P. Lambin, *Physical Review B*, 2013, **88**, 075427.
32 H. Zhan, G. Zhang, Y. Zhang, V. Tan, J. M. Bell and Y. Gu, *Carbon*, 2016, **98**, 232–237.
33 J. M. Marmolejo-Tejada, J. Fix, P. Kung, N. J. Borys and M. A. Mosquera, *Journal of Physical Chemistry C*, Accepted 2022.
34 W. Li, J. Carrete and N. Mingo, *Applied Physics Letters*, 2013, **103**, 253103.
35 X. Zhang, H. Xie, M. Hu, H. Bao, S. Yue, G. Qin and G. Su, *Physical Review B*, 2014, **89**, 054310.
36 R. Yan, J. R. Simpson, S. Bertolazzi, J. Brivio, M. Watson, X. Wu, A. Kis, T. Luo, A. R. Hight Walker and H. G. Xing, *ACS nano*, 2014, **8**, 986–993.
37 T. Kim, D. Ding, J.-H. Yim, Y.-D. Jho and A. J. Minnich, *APL Materials*, 2017, **5**, 086105.
38 X. Zhang, D. Sun, Y. Li, G.-H. Lee, X. Cui, D. Chenet, Y. You, T. F. Heinz and J. C. Hone, *ACS applied materials & interfaces*, 2015, **7**, 25923–25929.
39 X. Gu and R. Yang, *Applied Physics Letters*, 2014, **105**, 131903.
40 B. Peng, H. Zhang, H. Shao, Y. Xu, X. Zhang and H. Zhu, *RSC advances*, 2016, **6**, 5767–5773.
41 X. Liu, G. Zhang, Q.-X. Pei and Y.-W. Zhang, *Applied Physics Letters*, 2013, **103**, 133113.
42 V. Varshney, S. S. Patnaik, C. Muratore, A. K. Roy, A. A. Voevodin and B. L. Farmer, *Computational Materials Science*, 2010, **48**, 101–108.
43 A. Krishnamoorthy, P. Rajak, P. Norouzzadeh, D. J. Singh, R. K. Kalia, A. Nakano and P. Vashishta, *AIP Advances*, 2019, **9**, 035042.
44 N. Peimyoo, J. Shang, W. Yang, Y. Wang, C. Cong and T. Yu, *Nano Research*, 2015, **8**, 1210–1221.